J. Fluid Mech. (2020), *vol.* 888, A14. © The Author(s), 2020.
Published by Cambridge University Press
doi:10.1017/jfm.2020.19

Multifractal analysis of flame dynamics during transition to thermoacoustic instability in a turbulent combustor

Manikandan Raghunathan[1,†], Nitin B. George[2], Vishnu R. Unni[3], P. R. Midhun[1], K. V. Reeja[1] and R. I. Sujith[1]

[1]Department of Aerospace Engineering, Indian Institute of Technology, Madras 600 036, India

[2]Potsdam Institute for Climate Impact Research, P.O. Box 60 12 03, 14412 Potsdam, Germany

[3]Department of Mechanical and Aerospace Engineering, University of California San Diego, La Jolla, California 92093, USA

(Received 2 June 2019; revised 7 November 2019; accepted 2 January 2020)

Gas turbine combustors are susceptible to thermoacoustic instability, which manifests as large amplitude periodic oscillations in acoustic pressure and heat release rate. The transition from a stable operation characterized by combustion noise to thermoacoustic instability in turbulent combustors has been described as an emergence of order (periodicity) from chaos in the temporal dynamics. This emergence of order in the acoustic pressure oscillations corresponds to a loss of multifractality in the pressure signal. In this study, we investigate the spatiotemporal dynamics of a turbulent flame in a bluff-body stabilized combustor during the transition from combustion noise to thermoacoustic instability. During the occurrence of combustion noise, the flame wrinkles due to the presence of small-scale vortices in the turbulent flow. On the other hand, during thermoacoustic instability, large-scale coherent structures emerge periodically. These large-scale coherent structures roll up the wrinkled flame surface further and introduce additional complexity in the flame topology. We perform multifractal analysis on the flame contours detected from high-speed planar Mie scattering images of the reactive flow seeded with non-reactive tracer particles. We find that multifractality exists in the flame topology for all the dynamical states during the transition to thermoacoustic instability. We discuss the variation of multifractal parameters for the different states. We find that the multifractal spectrum oscillates periodically during the occurrence of thermoacoustic instability at the time scale of the acoustic pressure oscillations. The loss of multifractality in the temporal dynamics and the oscillation of the multifractal spectrum of the spatial dynamics go hand in hand.

Key words: fractals, turbulent reacting flows, vortex shedding

1. Introduction

Turbulent flow is ubiquitous in nature and is found across a wide range of systems that span simple flows, such as a flow in a coffee cup, to cosmological flows. The

† Email address for correspondence: manikandanraghu05@gmail.com

presence and significance of eddies of different length scales in turbulent flows have been studied extensively in the past few decades (Tennekes & Lumley 1972; Frisch & Kolmogorov 1995; Davidson 2015). Turbulent kinetic energy from the eddies of large length scales is transferred to lower but comparable length scales through nonlinear interactions. Eventually, the energy is dissipated as heat at the Kolmogorov length scales through viscous dissipation. This process of energy transfer across different length scales is referred to as the energy cascade (Richardson 1922; Pope 2000).

The nonlinear interaction between the eddies of multiple scales causes the flow to become chaotic (Aref 1983; McWilliams 1984). However, in some turbulent flows, we can observe an emergence of order from chaos characterized by the evolution of large-scale structures formed by the roll-up or merging of several small-scale structures. These large-scale organized structures are referred to as coherent structures (Ho & Nosseir 1981; McWilliams 1984).

Similar to the emergence of order from chaos in turbulent flows, other systems also exhibit transition to order. Spontaneous transition from chaos to order in biological systems, ecological systems etc., has been studied extensively using the theory of self-organization (Ball 1999; Camazine *et al.* 2003). Cross & Hohenberg (1993) present many examples of self-organization, both in temporal and spatial dynamics, in hydrodynamic systems such as Rayleigh–Bénard convection, Taylor–Couette flow etc.

Emergence of temporal order in systems which exhibit oscillatory instabilities often manifests as an emergence of periodicity in the temporal fluctuations of the state variable(s) of the system. Such an emergence of temporal order has been observed in aeroacoustic (Rockwell & Naudascher 1979; Rockwell 1983), aeroelastic (Fung 1955) and thermoacoustic systems (Zukoski 1985; Poinsot *et al.* 1987). In such systems, order emerges in the form of self-sustained periodic oscillations in their state variable(s).

In general, order can also emerge in the spatial domain in thermodynamically open systems, operating far from thermodynamic equilibrium. Emergence of such spatiotemporal order is often through spontaneous self-organization, achieved by the exchange of energy and matter with the external environment (Tiezzi *et al.* 2008). Examples of systems that exhibit such self-organization include Belousov–Zhabotinsky reaction, Bénard cells and droplet clusters (Tiezzi *et al.* 2008; Ciotti *et al.* 2011).

Such an emergence of order from chaos is observed in a turbulent thermoacoustic system during the transition from the state of combustion noise to thermoacoustic instability. The state of combustion noise corresponds to the stable operating regime of the combustor (Strahle 1978), while thermoacoustic instability corresponds to the unstable operating regime of the combustor. Thermoacoustic instability occurs due to a positive feedback between the unsteady heat release rate and the acoustic pressure oscillations and is characterized by large amplitude pressure oscillations which lead to excessive structural vibrations (Lieuwen 2012; Juniper & Sujith 2018).

Recent studies indicate that the transition states prior to thermoacoustic instability exhibit rich dynamic behaviour (Gotoda *et al.* 2011, 2015; Nair, Thampi & Sujith 2014; Unni & Sujith 2015; Pawar *et al.* 2017). A turbulent combustor exhibits the characteristics of a complex system during these states (Juniper & Sujith 2018; Unni *et al.* 2018). Results from these studies indicate that there is a gradual emergence of periodicity from aperiodicity in the temporal dynamics (Nair *et al.* 2014) and an emergence of order from disorder in the spatiotemporal dynamics during the transition from combustion noise to thermoacoustic instability via intermittency (Mondal, Unni & Sujith 2017; George *et al.* 2018; Premchand *et al.* 2019). During the occurrence of

intermittency, bursts of high amplitude periodic fluctuations appear amidst epochs of low amplitude aperiodic fluctuations in an apparently random manner.

The spatiotemporal dynamics of a turbulent combustor is largely influenced by the coupling between the various subsystems such as the hydrodynamic field, the reactive field (flame) and the acoustic field (Candel 1992). George *et al.* (2018) showed that the emergence of order from chaos during thermoacoustic instability is the result of interactions among the patterns formed in various subsystems. The patterns formed are the standing wave pattern in the acoustic field, the large-scale coherent structures in the flow field and the coherent patterns of the flame. They suggested that interactions between these subsystems are mediated by the emerging spatiotemporal patterns, leading to increased order or coherence in the combustion dynamics. For instance, they showed that collective interaction of small-scale vortices results in the formation of a large-scale vortex and leads to coherence in the flame.

Richardson's (1922) description of turbulent flows states that flows consist of a hierarchy of scales. Several studies showed that flow structures with multiple spatial scales in turbulent flows exhibit the characteristics of self-similarity (Meneveau & Sreenivasan 1986; Benzi *et al.* 1993). The self-similarity in turbulent flows has been studied using the theory of fractal geometry. For example, Mandelbrot (1983) suggested that turbulence involves several fractal facets. Fractal theory gives us a simple, geometrical interpretation of the complexity in the system.

The complexity exhibited by many spatially extended systems is due to the presence of multiple spatial and temporal scales. In such systems, a spectrum of fractal dimensions is required to characterize their complexity (Murcio *et al.* 2015). Such a system characterized by a set of fractal dimensions is referred to as a multifractal system. If a fractal can be described using a single fractal dimension, then it is called a monofractal. Otherwise, it is labelled as a multifractal (Engelking 1978; Pesin 2008). Examples of multifractal time series include human physiological signals (Ivanov *et al.* 1999; Ihlen & Vereijken 2013), geoelectric signals (Telesca *et al.* 2003) and seismic signals (Telesca *et al.* 2015). Multifractal description was first introduced by Mandelbrot to study the fractal characteristics of turbulent flows (Mandelbrot 1974). Meneveau & Sreenivasan (1991) experimentally showed that the kinetic energy dissipation field in a turbulent flow has a multifractal distribution which supports the notion of a self-similar multiplicative fragmentation process occurring in the energy cascade.

For a swirl-stabilized turbulent combustor, Gotoda *et al.* (2012) showed that the acoustic pressure oscillations prior to lean blowout exhibit multifractal characteristics. In addition, they also emphasized that multifractal analysis is indeed necessary to capture the rich dynamics observed in the pressure oscillations near to the blowout. For bluff-body stabilized and swirl-stabilized turbulent combustors, Nair & Sujith (2014) reported that the unsteady pressure oscillations exhibit multifractality due to the presence of fluctuations of multiple temporal scales during the occurrence of combustion noise. Further, they showed that there is a loss of multifractality in the unsteady pressure oscillations when the combustion dynamics transitions from combustion noise to thermoacoustic instability. This loss of multifractality was attributed to a reduction of multiple time scales to a few discrete time scales associated with the formation of a large-scale coherent structure during the occurrence of thermoacoustic instability. However, the above studies did not discuss the multifractal characteristics associated with the flame dynamics.

In the present work, we study multifractality of the flame topology as the dynamical state of a turbulent thermoacoustic system transitions from combustion noise to thermoacoustic instability via intermittency. We observe small-scale vortical structures during the occurrence of combustion noise and a wide range of spatial scales during the occurrence of thermoacoustic instability. We show that the turbulent flame topology exhibits multifractality during the different dynamical states. Even during the occurrence of thermoacoustic instability when there is an existence of ordered temporal dynamics, the spatial topology of the flame is multifractal. We show that periodic oscillations of the multifractal spectrum of the flame topology result in the periodic oscillations of the heat release rate.

The paper is organized as follows: § 2 presents a background of the multifractal formalism. Section 3 provides the details of the experimental set-up and the data acquisition systems used in this study. Section 4 discusses the results from the experimental study. Section 5 presents the key findings of the study. A comparison of the turbulent spatial scales with other spatial scales in the system, methodology to detect the flame contours, the estimation of the multifractal spectrum and the uncertainties estimation in the calculation of multifractal parameters are elaborated in the appendices A–D, respectively.

2. Multiplicative cascade processes and multifractality

Many natural processes such as cloud formation, nuclear chain reaction, turbulent flows, redistribution of human population across the globe, biological evolution etc., involve multiplicative cascade processes (Schertzer *et al.* 1997; Cheng 2014). A multiplicative cascade process is characterized by iterative transformations of a system resulting in the redistribution of a measure of the system across its topology. Here, the measure is any quantifiable property of the system such as population density, concentration of a species, energy density etc., that varies across the topology of the system. A famous example of a multiplicative cascade process is the turbulent energy cascade (Richardson 1922). The multiplicative cascade process often results in a fractal or multifractal distribution of a measure across the topology of a system (Martínez *et al.* 1990).

Fractals are geometric objects that are self-similar across different scales. Measures such as length and area of a fractal are dependent upon the scale of the measurement. A log–log plot of a measure of the fractal with the scale of the measurement gives a straight line with a non-integer slope of negative fractal dimension. In systems with heterogeneous distribution of measures such as the distribution of copper ore in the earth's crust (Mandelbrot 1989), distribution of rainfall and clouds across the atmosphere (Lovejoy & Schertzer 1991), the scaling behaviour can vary from one part of the system to another. For such systems, a single fractal dimension is inadequate to explain the local scaling behaviours of the measure and a multifractal description is needed to represent the complexity in the scaling. Often, in spatiotemporal systems, the local fractal dimension could vary in space due to the localized irregularities in the field, making them multifractal (Dauphiné 2013).

Classical statistical properties such as variance, skewness and kurtosis, represent the statistical dispersion of a measure. However, these properties do not account for the non-stationarity and the non-homogeneity in the distribution of a measure. In multifractal analysis, it is possible to determine the irregularities and discontinuities present in the spatial distribution of a measure. A multifractal spectrum represents all such irregularities, large or small, across all scales of the measure, based on

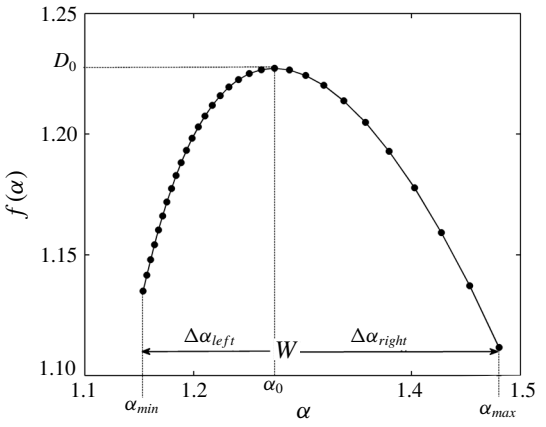

FIGURE 1. The singularity spectrum $f(\alpha)$ is plotted as a function of the singularity exponent α. The singularity spectrum is obtained by performing multifractal analysis on a typical flame image obtained in our experiments. The parameters D_0, α_0, $\Delta\alpha_{right}$, $\Delta\alpha_{left}$ and W define the multifractal spectrum.

the scaling of different orders of moments of the distribution of the measure (Salat, Murcio & Arcaute 2017). In this study we use a multifractal spectrum known as the singularity spectrum, obtained using the box-counting method, to study the multifractal characteristics of the flame topology.

In a multifractal field G, a measure (μ) which characterizes the topology of G varies in space. A mathematical description of measure μ is explained in appendix C. Consider a region of radius, ε around any point, x_0 in G. The measure μ within the region of radius ε has a power-law relation with ε, when the range of ε is sufficiently small (Chhabra & Jensen 1989). Accordingly, the relation between μ and ε is given as

$$\mu(\varepsilon) \sim \varepsilon^{\alpha}, \tag{2.1}$$

where the scaling exponent α is known as the Lipschitz–Hölder exponent. The exponent α represents the strength of the local scaling of the distribution of μ around x_0, otherwise known as the singularity exponent at x_0. Since G is multifractal, α is a function of x_0. The distribution of α in G is characterized by $f(\alpha)$, which is the fractal dimension (Hausdorff dimension) corresponding to the set of points in G with a singularity exponent α. The fractal dimension $f(\alpha)$ for a given α is determined based on the number of regions $N_\alpha(\varepsilon)$ of radius ε that form the set with the same α and is given as,

$$N_\alpha(\varepsilon) \sim \varepsilon^{-f(\alpha)}. \tag{2.2}$$

In the present work, we compute α and $f(\alpha)$ following the method described by Chhabra & Jensen (1989). The steps for the estimation of α and $f(\alpha)$ are explained in appendix C. In our analysis, μ is selected as the normalized probability mass distribution of the non-zero pixel intensity in the flame image (Giri *et al.* 2014).

The multifractal spectrum provides a mathematical description of multifractality in terms of $f(\alpha)$ and α. Figure 1 shows the representative multifractal spectrum resulting from the multifractal analysis on a flame image acquired in our experiments. The shape and the position of the spectrum represents the range of fractal dimensions required to describe the system and the relative dominance of each fractal dimension

in determining its topology. For the case of monofractals, the multifractal spectrum reduces to a point as α becomes constant everywhere.

The four parameters namely, the capacity dimension D_0, the spectrum width W, the most dominant singularity exponent α_0 (value of α at which $f(\alpha)$ is maximum) and the asymmetry parameter B are used to characterize the multifractal spectrum (Telesca *et al.* 2003). The maximum value of $f(\alpha)$ is the capacity dimension (D_0) which quantifies the space-filling nature of the fractal. For example, a fractal curve that lies in a two-dimensional (2-D) plane is said to be space-filling if the curve is highly wrinkled and hence covers most of the area of the 2-D plane. The D_0 of such a 2-D fractal object lies in the interval between 1 and 2. A high value of D_0 close to 2 indicates that the space is almost entirely occupied by the fractal (Lopes & Betrouni 2009). Conversely, D_0 reduces to 1 for a line segment. We further state that the capacity dimension or the box-counting dimension (calculated using the box-counting method) takes the same value as the Hausdorff dimension, when the fractal satisfies the open set condition (Wagon 2010).

The width of the spectrum defined as $W = \alpha_{max} - \alpha_{min}$, represents the range of scaling exponents found in the multifractal field G. The larger the value of W, the wider the range of scaling exponents present in G. The most dominant singularity exponent α_0 represents the most probable singularity over the support of G (Goltz 1996; Giri *et al.* 2014). A high value of α_0 indicates a higher probability of regions of densely concentrated μ over the support of G. Conversely, a low value of α_0 indicates a high probability of regions of sparse distribution of μ over the support of G.

The asymmetry parameter B describes the skewness of the spectrum based on $\Delta\alpha_{right}$ and $\Delta\alpha_{left}$, where $\Delta\alpha_{right}$ is given as $\alpha_{max} - \alpha_0$ and $\Delta\alpha_{left} = \alpha_0 - \alpha_{min}$. The asymmetry parameter is defined as $B = \Delta\alpha_{right} - \Delta\alpha_{left}$. The spectrum is symmetric if $B = 0$, left-skewed if B is negative and right-skewed if B is positive. A right-skewed spectrum indicates more irregularity within the smaller spatial structures. Conversely, a left-skewed spectrum indicates higher irregularity within the larger spatial structures.

In the present work, we estimate the values of D_0, α_0, W and B of the flame contours. These flame contours are extracted from the Mie scattering images of the reactive flow. The flame contains wrinkles which are heterogeneously distributed. We study the spatial distribution of these wrinkles in the flame during the different dynamical states. The above-mentioned multifractal parameters can be used to describe the multifractal characteristics of the flame. The capacity dimension D_0 represents the space-filling nature of the flame inside the combustor. A high value of D_0 indicates that wrinkles in the flame occupy a larger area in the combustor. The most dominant singularity exponent α_0 represents how the distribution of wrinkles is present over the flame. A high value of α_0 indicates a heterogeneous concentration of wrinkles, with certain regions having dense concentration compared to other regions. The width of the spectrum demonstrates the range of scaling required to describe the distribution of wrinkles in the flame. A larger value of W implies that a wider range of scaling exponents is required to describe the distribution of wrinkles. The skewness indicates the dominance of irregularities either for the smaller length scales or for the larger length scales.

3. Experimental set-up

Experiments were performed on a turbulent combustor where the flame is stabilized using a circular bluff-body, at high Reynolds numbers ($Re > 18\,000$). The turbulent combustor used for the present study is shown in figure 2. The turbulent combustor

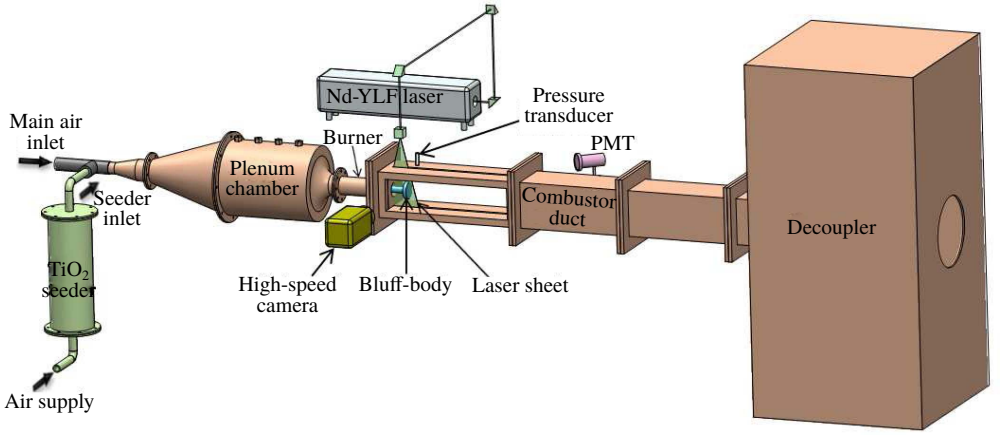

FIGURE 2. Schematic of the turbulent combustor used in this study. A piezoelectric pressure transducer measures the acoustic pressure fluctuations (p') whereas a photomultiplier (PMT) records the global heat release rate ($\dot{q}$). Mie scattering images of seeding particles (TiO_2), in a reactive flow are captured using a high-speed camera.

consists of a plenum chamber, a burner and a combustion chamber with extension ducts. A central shaft of diameter 16 mm through the burner supports the bluff-body. The central shaft is also used to deliver fuel into the combustion chamber through four radial injection holes of diameter 1.7 mm. The fuel is injected 120 mm upstream of the bluff-body. The bluff-body is a circular disk of diameter 47 mm and thickness 10 mm. The bluff-body is located at a fixed position of 35 mm from the backward facing step of the combustor. A disk of 2 mm thickness with 300 holes of diameter 1.7 mm each, located 30 mm downstream of the location of fuel-injection acts as a flashback arrestor. The combustion chamber consists of a sudden expansion from the circular burner of diameter 40 mm into a square geometry of cross-section 90 mm $\times$ 90 mm and length 1100 mm. A spark plug with a step-up transformer is mounted near the dump plane for ignition of the fuel–air mixture. We use liquefied petroleum gas (60 % butane and 40 % propane) as the fuel. A blow-down mechanism is used to supply air from high-pressure tanks. The air is passed through a moisture separator before it enters the plenum chamber.

The mass flow rates of air and fuel are controlled and measured using mass flow controllers (Alicat Scientific, MCR Series) with an uncertainty of $\pm$ (0.8 % of reading $+0.2$ %) of full scale. The Reynolds number for the reactive flow is computed using the expression $Re = 4\dot{m}/\pi\mu_a(d_o - d_i)$, where $\dot{m} = \dot{m}_a + \dot{m}_f$ is the mass flow rate of the air–fuel mixture, d_o is the diameter of the burner, d_i is the diameter of the bluff-body shaft and μ_a is the dynamic viscosity of the air–fuel mixture at the experimental conditions (Holman 1989). Further, the total mass flow rate of air for the combustion is given as $\dot{m}_a = \dot{m}_s + \dot{m}_m$, where $\dot{m}_s$ and $\dot{m}_m$ are the mass flow rates of the seeded and unseeded air streams, respectively. Corrections to Reynolds number due to the change in viscosity for the varying air–fuel ratios are performed, the procedure for which can be found in Wilke (1950). The Reynolds numbers for the reported experiments are $Re = 1.88 \times 10^4 \pm 574$ (combustion noise), $2.2 \times 10^4 \pm 630$ (intermittency) and $3.15 \times 10^4 \pm 889$ (thermoacoustic instability). The required Reynolds number is achieved by maintaining a constant fuel flow rate (30 standard litres per minute) and increasing the air flow rate. In this study, we discuss the results obtained at different equivalence

ratios (ϕ). The global equivalence ratio is calculated as $(\dot{m}_f/\dot{m}_a)_{actual}/(\dot{m}_f/\dot{m}_a)_{stoichiometry}$. The uncertainty present in the equivalence ratio is ± 0.02 based on the uncertainties in the mass flow controllers.

To maintain a certain level of consistency in the environmental conditions, experiments were performed when the acoustic damping rate is $19\ s^{-1} \pm 15\,\%$. The unsteady pressure signals are acquired using piezoelectric pressure transducers (PCB103B02, uncertainty ± 0.15 Pa). This pressure transducer is mounted at a distance of 25 mm from the dump plane of the combustor as shown in figure 2. A photomultiplier (PMT) (Hamamatsu H10722-01) with an *OH** filter (narrow bandwidth filter centred at 310 nm and 12 nm full width at half maximum) mounted in front of it, is used to capture the chemiluminescence intensity which is indicative of the global heat release rate within the combustor (Hardalupas & Orain 2004). The PMT is positioned such that the intensity of chemiluminescence from the entire flame in the combustion chamber is captured. Both the pressure signal from the pressure transducer and the global heat release rate from the PMT are acquired using an analogue-to-digital card (NI-6143, 16 bit) for a duration of 3 s with a sampling rate of 20 kHz. The acquisition of the pressure signals, PMT signals and camera images is synchronized using a signal generator (Tektronix-AFG1022, 25 MHz).

We acquired simultaneous 2-D planar Mie scattering images, acoustic pressure and global heat release rate measurements at different values of ϕ from stoichiometric conditions to leaner conditions. Thermoacoustic instability is observed at leaner conditions. For the 2-D planar Mie scattering technique, we use a single-cavity double-pulsed Nd:YLF laser (Photonics) of operating wavelength 527 nm to illuminate the seeding particles. The laser is operated at a repetition rate of 2 kHz in single pulse mode. A laser sheet of 2 mm thickness is created by expanding the laser beam using a spherical lens of focal length 600 mm and a plano-concave cylindrical lens of focal length -15 mm. This laser sheet is transmitted through a rectangular quartz window through the top plate of the duct into the combustion chamber.

We use TiO_2 (Kronos make-product-1071) particles of approximate size 1 μm to seed the flow. To have an adequate supply and uniform distribution of TiO_2 in the flow, a portion of the main air is diverted through a fluidized bed seeder where TiO_2 particles are mixed well with the incoming air. Subsequently, air with a homogeneous distribution of TiO_2 particles re-enters the main flow upstream of the plenum chamber. The mass flow rate of the seeded airflow ($\dot{m}_s$) is suitably adjusted for different equivalence ratios to provide an optimal supply of seeding particles to the flow. The supply of seeded air from the seeder into the experimental rig is shown in figure 2. These TiO_2 particles scatter light while they pass the plane illuminated by the laser sheet and this light is captured by the high-speed camera. The gas density changes across the flame, which in turn results in a density gradient of TiO_2 particle across the flame. Thus, the strong gradient of TiO_2 particle density in the reactive flow indicates the topology of the flame (Stella *et al.* 2001). In the past, many experimental studies have used similar Mie scattering technique to study flame dynamics (Nair & Lieuwen 2007; Hong *et al.* 2013).

The illuminated light from seeding particles in the reactive field is imaged using a high-speed camera (Photron SA4) which is synchronized with the Nd:YLF (527 nm) laser at 2000 fps. The camera is equipped with a Zeiss 100 mm lens and a short bandpass optical filter (527 ± 12 nm) to capture the scattered light from the seeding particles. The resolution of the camera is set as 1024×736 pixels throughout the experiments to capture the flame dynamics present in the top half of the combustor (45 mm $\times$ 34 mm) between the dump plane and the bluff-body. Mie scattering images

are acquired for a duration of 1.9 s for each experiment. Experiments are performed for three different dynamical states namely, combustion noise ($\phi = 0.94$), intermittency ($\phi = 0.75$) and thermoacoustic instability ($\phi = 0.6$).

4. Results

In this section, we discuss the qualitative and quantitative differences in the flame dynamics for the states of combustion noise, intermittency and thermoacoustic instability by performing a multifractal analysis of the flame topology. The spatial dynamics of the flame is influenced by vortices of different sizes that cause flame roll-up. Based on the scale of the roll-up, we refer to them as small-scale, medium-scale and large-scale. We identify the roll-up of the flame by the visual observation of the Mie scattering images. The normalized diameters (with respect to the combustor step size of 25 mm) of small-scale, medium-scale and large-scale roll-ups/vortices referred to in the following sections are $\sim$0.08, $\sim$0.24 and $\sim$0.6, respectively. The temporal statistics of the multifractal measures converge for 100 flame images. Hence, the values of the multifractal measures are obtained by analysing 100 flame images for each dynamical state. The calculation of uncertainty in the estimation of all multifractal measures for all dynamical states is discussed in appendix D.

4.1. *Multifractal analysis of the flame during combustion noise*

The turbulent flow field in a backward-facing step combustor consists of a reattachment mixing layer behind the step, which facilitates combustion. Within the mixing layer, discrete small-scale vortical structures are present, which entrain and mix the incoming reactants with the hot products from the reaction (Keller *et al.* 1982; Zukoski 1985; Renard *et al.* 1999). This entrainment and mixing process helps to provide continuous energy to ensure the ignition of the incoming reactants which, in turn, helps to stabilize the flame inside the combustor. Figure 3(I) represents the Mie scattering images during the occurrence of combustion noise ($\phi = 0.94$) at different instants of time (*a–c*). In this figure, from the roll-up of the flame, we can discern that small-scale vortical structures exist (marked by purple circles) within the mixing layer. George *et al.* (2018) showed that such small-scale vortical structures cause spatial and temporal incoherence in the acoustic power production.

Figure 3(II) shows the contours of the flame in the region of interest marked in figure 3(I-*a*). The flame contours are obtained after applying a suitable edge detection technique described in appendix B. The flame undergoes wrinkling due to the perturbation by small-scale vortices which is evident from figure 3(II). Further, we see that these wrinkles are heterogeneously distributed along the flame. When compared to figure 3(II-*b*), figures 3(II-*a*) and 3(II-*c*) show higher values of D_0 which can be attributed to the increased irregularities/wrinkling in the flame contour at those time instants. Many studies have previously reported that a 2-D turbulent premixed flame structure exhibits fractal behaviour during stable operation with a mean value of D_0 between 1.13 and 1.32 (North & Santavicca 1990; Gülder *et al.* 2000). To obtain a quantitative description of the presence of wrinkles and their heterogeneous distribution, we use multifractal analysis.

We show the temporal variation of D_0, α_0 and acoustic pressure fluctuations (p') along with global heat release rate fluctuations ($\dot{q}'$) during the occurrence of combustion noise in figure 4(*a–c*), respectively. Now, D_0 fluctuates around a mean value of 1.22 with maximum and minimum value of 1.31 and 1.17, respectively. The

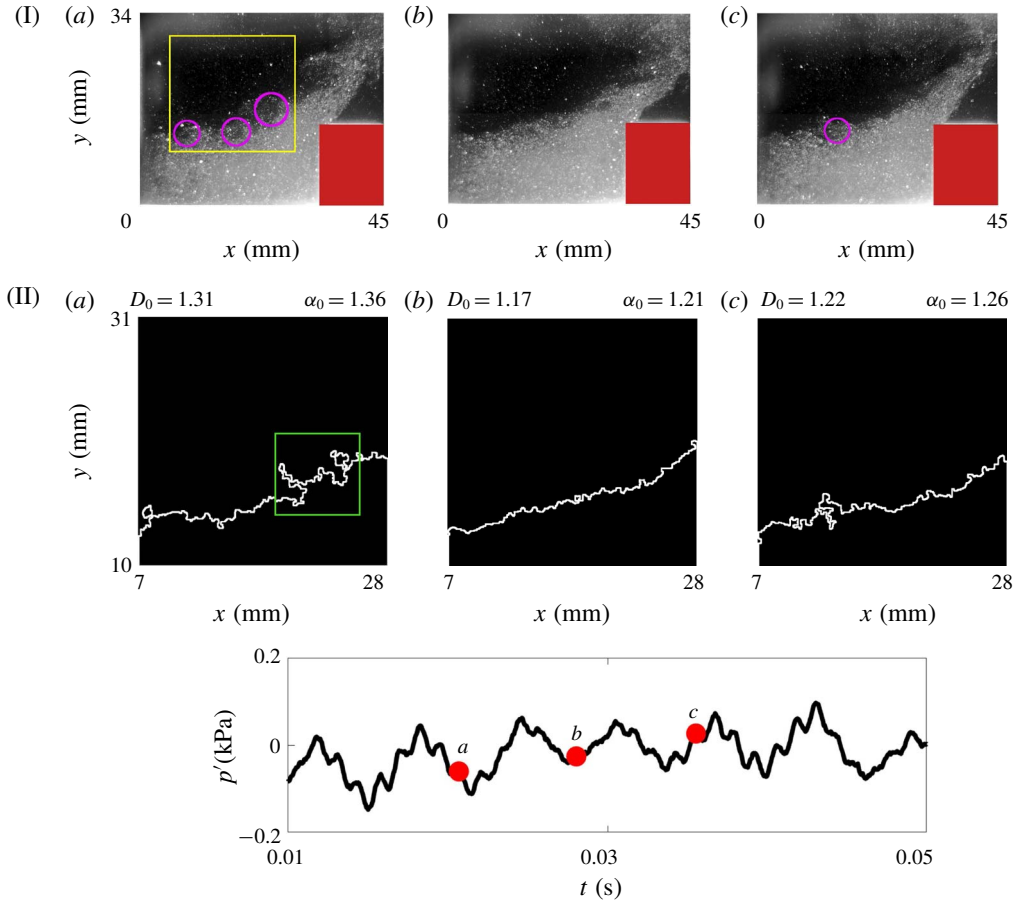

FIGURE 3. (I) Mie scattering images acquired during the occurrence of combustion noise at $\phi = 0.94$ ($Re = 1.88 \times 10^4$) for different instants of time (a–c). The bluff-body is represented by the red rectangle in (I). Small-scale roll-ups are marked with purple circles. The normalized diameter of these small-scale roll-ups is ∼0.08. Edge detection is performed on the selected region of interest which has a cross-sectional area of 21 mm × 21 mm, shown in (I) enclosed by the yellow square, to detect the flame contours. We choose this region of interest to capture and compare the spatiotemporal dynamics that occur at different dynamical states and to avoid the regions where substantial reflection of laser light from the bluff-body and the combustor walls is present. Subsequently, multifractal analysis is performed on the detected flame contours. The corresponding values of D_0 and α_0 for each flame are shown in (II). Acoustic pressure fluctuations corresponding to the images of (I) and (II) are shown in (III).

low value of D_0, close to 1 indicates that the flame is not space-filling. In other words, the flame contour fails to fill the area within the region of interest, marked by the yellow square.

In figure 4(b), we can observe that α_0 fluctuates around a mean value of 1.26 with a maximum and a minimum value of 1.36 and 1.16, respectively. A higher value of $\alpha_0 = 1.36$ when compared to $\alpha_0 = 1.16$ denotes the presence of a dense concentration of wrinkles at certain parts of the flame contour. In other words, a higher value of α_0 indicates a more heterogeneous distribution of irregularity in the flame topology.

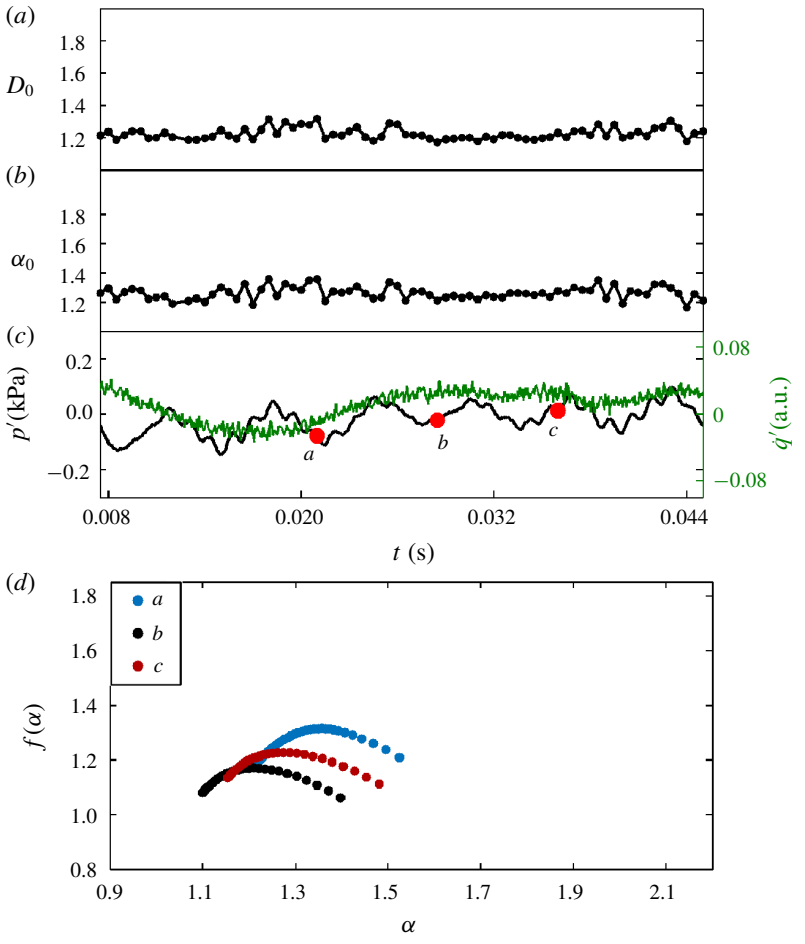

FIGURE 4. Time trace of D_0 (*a*), α_0 (*b*) and the corresponding p' (black line) along with $\dot{q}'$ (green line) (*c*) during the state of combustion noise is shown. The variation of $f(\alpha)$ with respect to α at different instants of time (*a–c*) is shown in (*d*).

One such example is the flame in figure 3(II-*a*) which gives the value of $\alpha_0 = 1.36$. Here, the region marked by the green square shows a part of the flame which is more irregular compared to other parts of the flame. Comparison of figures 4(*a*) and 4(*b*) shows that α_0 follows a similar trend as D_0 which indicates that the flame exhibits a space-filling character along with an increase in the heterogeneity of the distribution of wrinkles on the flame.

Next, we show the variation of the multifractal spectrum $f(\alpha)$ with respect to the singularity strength α for the flame contours shown in figure 3(II) in figure 4(*d*). We observe that all three spectra are right skewed. The right-skewed spectrum indicates a dominant presence of small-scale wrinkles on the flame. The mean value of the width of the multifractal spectrum W is approximately 0.28. To summarize, during the occurrence of combustion noise, we obtain a right-skewed spectrum with the temporal mean value of $D_0 = 1.22$, $\alpha_0 = 1.26$ and $W = 0.28$. This indicates low space-filling by the flame and a scattered distribution of small-scale wrinkles along the flame contour.

4.2. *Multifractal analysis of the flame during intermittency*

During the state of intermittency, the flame exhibits two distinct spatiotemporal dynamics. We either observe aperiodic wrinkling of the flame, or a periodic roll-up of the flame. The aperiodic wrinkling of the flame is due to the inherent turbulent fluctuations in the flow while the periodic roll-up is the result of an emergence of large-scale coherent structures in the shear layer. Small aperiodic perturbations at the flame root (anchoring point of the flame) propagate along the flame, causing aperiodic oscillations up to the flame tip. These aperiodic oscillations along the flame further result in aperiodic oscillations of the acoustic pressure fluctuations (Shanbhogue *et al.* 2009; Unni & Sujith 2017). The acoustic pressure oscillates aperiodically until the amplitude of the perturbation exceeds a critical value.

Figure 5(I) shows the instantaneous Mie scattering images acquired during an aperiodic epoch of intermittency ($\phi = 0.75$). In figure 5(I), we observe vortices of multiple spatial scales marked by purple circles. The spatial dynamics of the flame during the aperiodic epochs of intermittency exhibits characteristics similar to that of combustion noise (refer figure 3-I). However, the size of the roll-up ranging from small-scale to medium-scale during the aperiodic epochs of intermittency is slightly larger compared to the roll-up during the occurrence of combustion noise shown in figure 3(I). In figure 5(II-*a–c*), we observe that medium-scale wrinkles coexist with small-scale wrinkles.

The instantaneous Mie scattering images and the corresponding flame contours in the region of interest during one acoustic cycle of a periodic epoch of intermittency are shown in figure 6(I) and 6(II), respectively. We observe large-scale roll-up in the flame, as seen in figure 6(II-*b* and II-*c*). Within the large-scale roll-up, there are small-scale roll-ups caused by small-scale vortical structures, suggestive of collective interaction (Ho & Nosseir 1981; George *et al.* 2018). During collective interaction, small-scale vortices interact with each other, resulting in the self-organization and order at a larger scale, forming a large-scale coherent structure. These large-scale coherent structures along with small-scale vortical structures stretch the flame, resulting in an increase in the flame surface area, which leads to more intense chemical reactions (Kim *et al.* 2009).

The temporal variation of D_0, α_0 and p' along with $\dot{q}'$ corresponding to the aperiodic and periodic epochs of intermittency is shown in figures 7(*a–c*) and 7(*e–g*), respectively. In the case of the aperiodic epoch, D_0 fluctuates around a mean value of 1.19 with a maximum of 1.43 and a minimum of 1.08. This mean value of D_0 is slightly less than that observed for combustion noise. The lower value of D_0 during the aperiodic epoch of intermittency indicates that the flame undergoes relatively less wrinkling and is relatively smoother and more regular compared to the flames seen during the occurrence of combustion noise. From figure 7(*b*), we see that during the aperiodic epochs of intermittency, α_0 fluctuates around a mean value of 1.24 with a maximum of 1.47 and minimum of 1.10. The mean value of α_0 has also slightly decreased from the state of combustion noise to the aperiodic epoch of intermittency.

On the other hand, during the periodic epochs of intermittency, the mean value of D_0 increases to 1.28 with an increase in the maximum and the minimum values to 1.58 and 1.12, respectively, as shown in figure 7(*e*). The overall increase in the value of D_0 is a result of enhanced space filling of the flame due to the presence of a large-scale vortex structure and the small-scale vortical structures within it. The space-filling nature of the flame due to increased wrinkling corresponds to larger mixing of the reactants and hot radicals. The large-scale coherent structure breaks into small structures by impinging on the bluff-body and produces a significant heat release rate

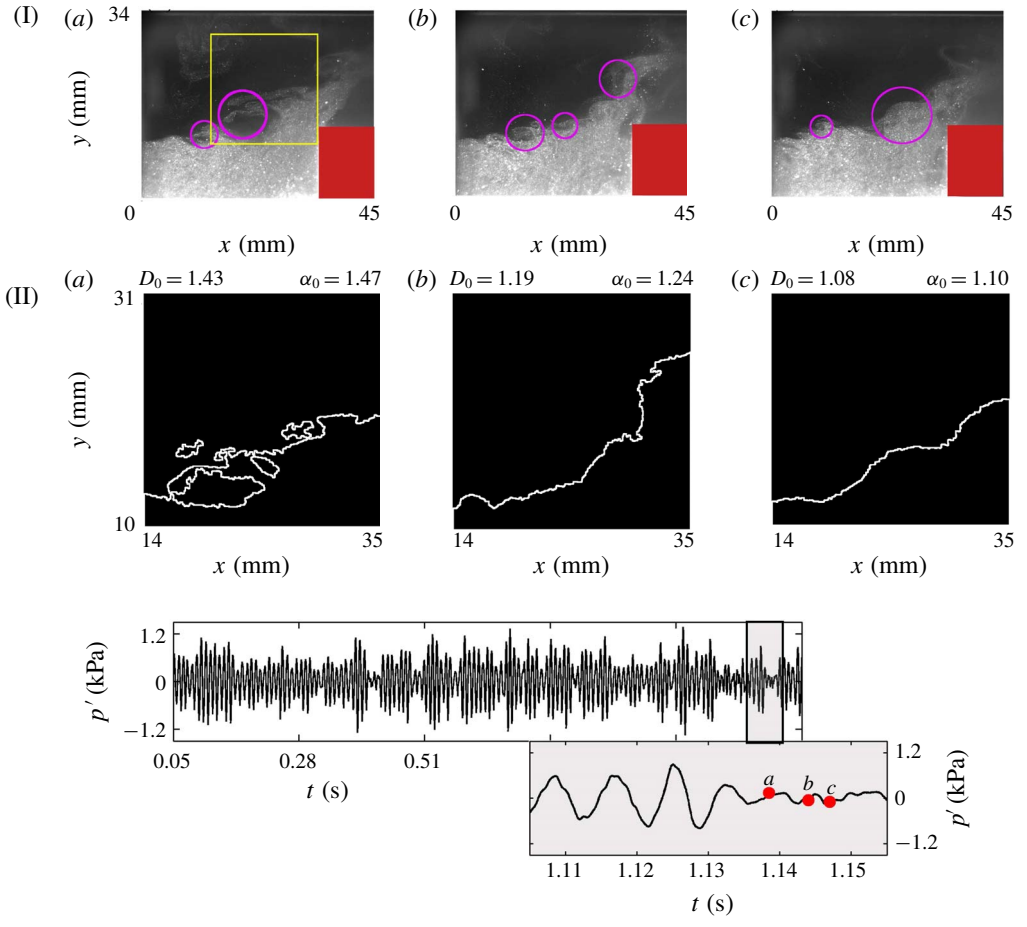

FIGURE 5. Mie scattering images acquired during an aperiodic epoch of intermittency at $\phi = 0.75$ ($Re = 2.2 \times 10^4$) are shown in (I) for different instances (*a–c*). The roll-ups of different spatial scales are marked with purple circles. The medium scale roll-up marked in (I-*a*) is ∼0.24 normalized diameter in size. The region of interest marked by the yellow square in (I-*a*) is different from the region of interest chosen for combustion noise. The region of interest is shifted approximately 7 mm to the right to capture the largest scale of the roll-up during periodic epochs of intermittency. The detected flame contours from the Mie scattering images are shown in (II) along with the corresponding values of D_0 and α_0. The time series of acoustic pressure fluctuations with a zoomed section of the aperiodic epoch is shown in (III). The acoustic pressure fluctuations corresponding to these Mie scattering images are marked in (III).

($\dot{q}'$). In addition, D_0 oscillates periodically, which is due to the periodic emergence of the large-scale coherent structure.

The mean value of α_0 is 1.32 and it oscillates periodically between the maximum and the minimum values of 1.62 and 1.11, respectively, as shown in figure 7(*f*). Also, α_0 reaches its maximum value when the large-scale coherent structure is at its maximum size (refer figure 6II-*b*). This high value of α_0 suggests that the large-scale coherent structure contains more regions of dense concentration of irregularities in the flame contour caused by the small-scale vortices. Also, D_0 and α_0 increase simultaneously. This indicates that the flame fills the space through wrinkles of

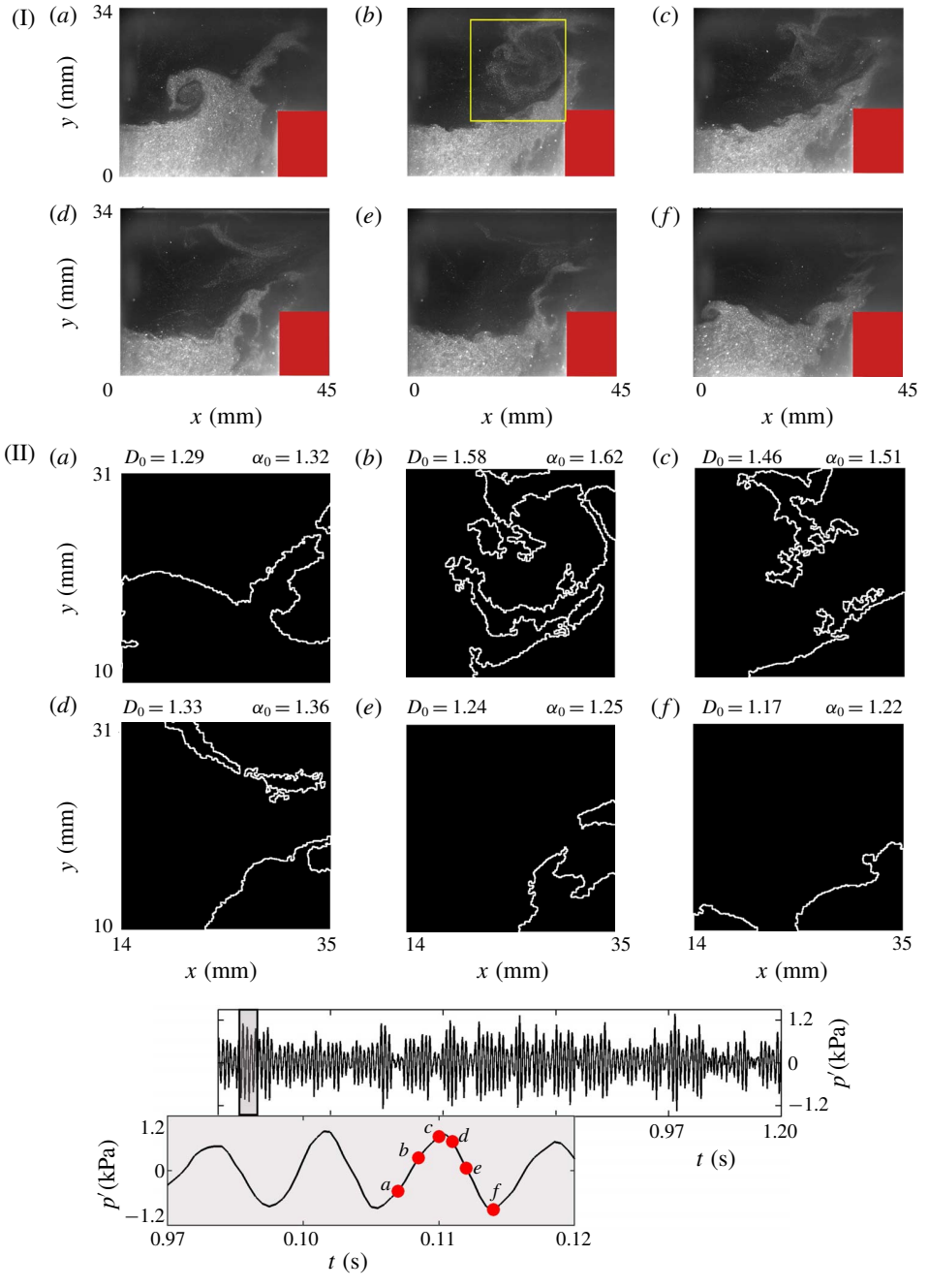

FIGURE 6. Mie scattering images acquired during the occurrence of a periodic epoch of intermittency at $\phi = 0.75$ for different instances are shown in (I). The largest spatial structure is captured within the region of interest marked by the yellow square in (I-*b*). The corresponding flame contours are shown in (II) along with the corresponding values of D_0 and α_0. The flame rolls-up to form large-scale coherent structures during the periodic epochs of intermittency as seen in (II-*b*) and (II-*c*). The time series of acoustic pressure fluctuations with a zoomed section of the periodic epoch is shown in (III). The acoustic pressure fluctuations corresponding to these Mie scattering images are marked in (III).

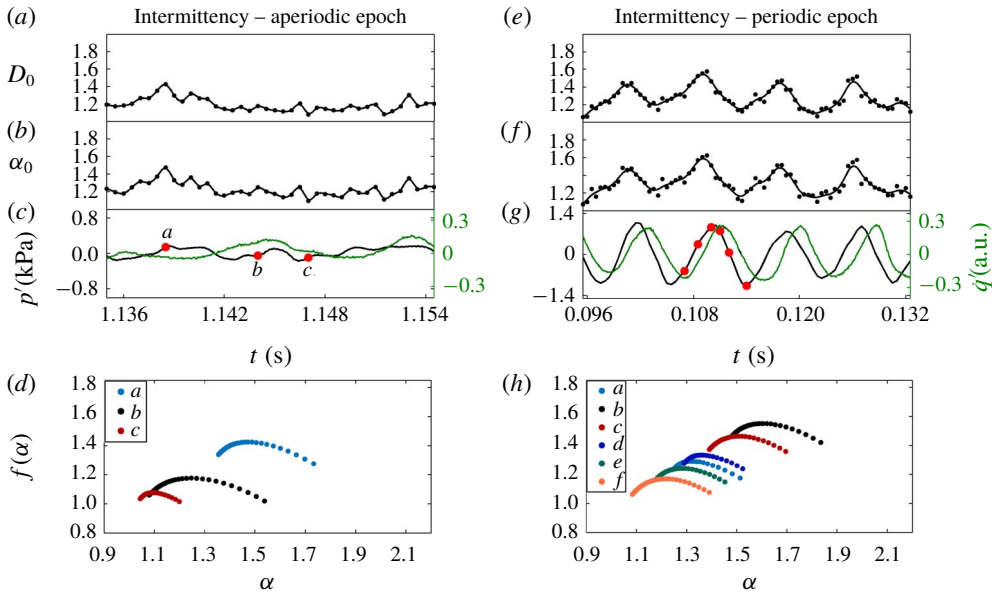

FIGURE 7. Time trace of D_0, α_0 and the corresponding p' (black line) along with $\dot{q}'$ (green line) during the aperiodic and the periodic epochs of intermittency are shown in (*a–c*) and (*e–g*), respectively. D_0 and α_0 fluctuate aperiodically during the aperiodic epochs of intermittency while they oscillate periodically with a higher mean value during the periodic epoch. The singularity spectra obtained at different instants of time during aperiodic and periodic epochs of intermittency are shown in (*d*) and (*h*), respectively.

larger size along with an increase in the number of small-scale wrinkles within the large-scale structure, suggestive of collective interaction. The multifractal spectra calculated at different instances during the aperiodic epochs of intermittency for the flame contours shown in figure 5(II) are shown in figure 7(*d*). Similar to the spectra during the occurrence of combustion noise, these spectra are right-skewed, which is indicative of irregularities dominant at the smaller scales, which demonstrates the presence of small-scale wrinkles. The mean value of W is approximately 0.28, which is the same value of W observed during the state of combustion noise.

The multifractal spectrum for the flame corresponding to the periodic epochs of intermittency is shown in figure 7(*h*). In general, there is a rightward shift of the multifractal spectrum for the periodic epochs of intermittency as compared to those of the aperiodic epochs. The spectrum shifts to the right due to an increase in α_0. This increase in α_0 implies a higher heterogeneity in the spatial dynamics, which is due to the presence of a higher number of small-scale structures within the large-scale structure. Further, the multifractal spectrum shifts periodically from left to right and bottom to top during the periodic epochs of intermittency, which characterize the periodic emergence of large-scale coherent structure. The bottom to top oscillation of the multifractal spectrum corresponds to the periodic oscillation of the space-filling character of the flame. In general, the multifractal spectra are right-skewed and the mean value of W is also around 0.28 for the periodic epoch of intermittency.

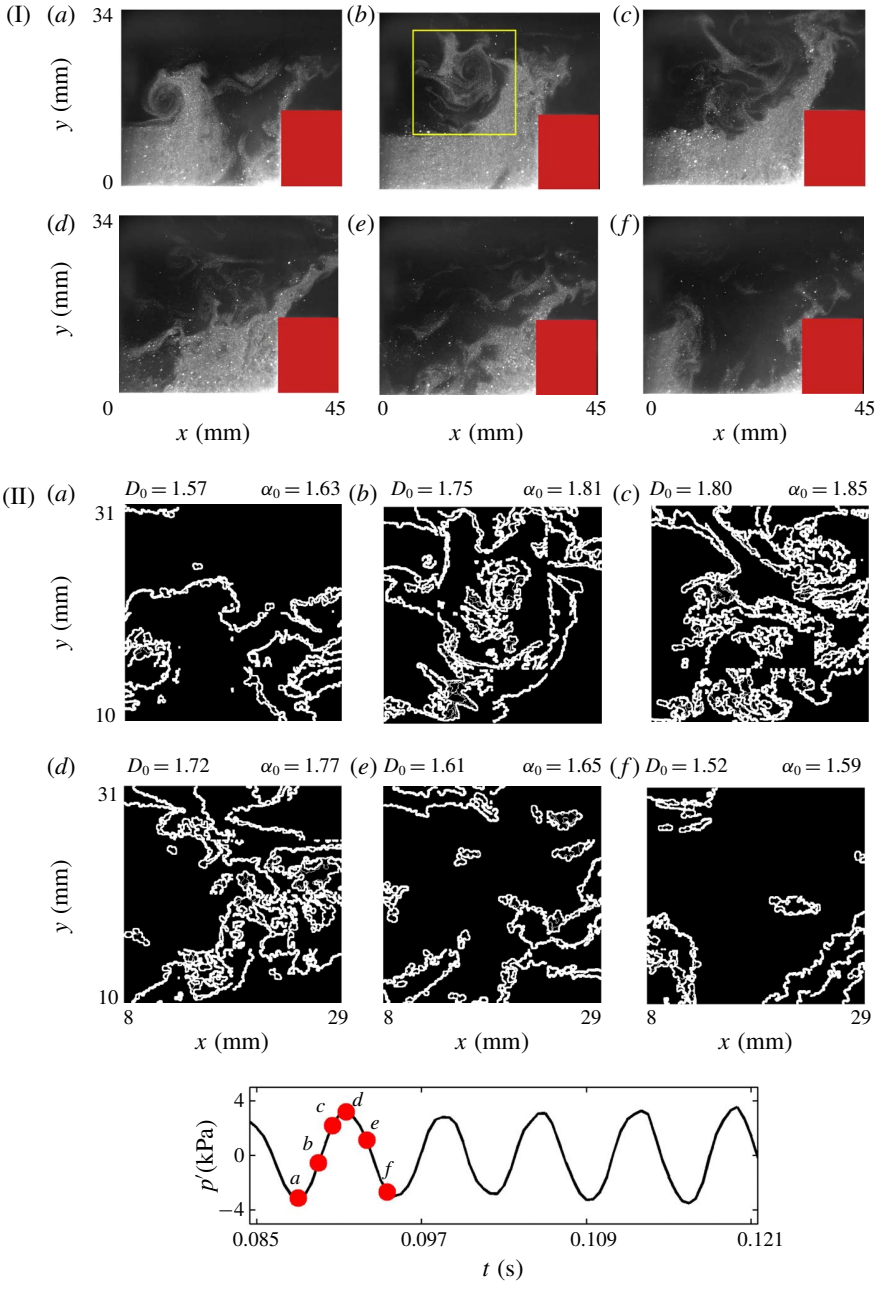

FIGURE 8. Mie scattering images acquired during one cycle of thermoacoustic instability at $\phi = 0.6$ ($Re = 3.15 \times 10^4$) for different instants of time are shown in (I). The large-scale roll-up (normalized diameter ∼0.6) observed in (II-*b* and II-*c*) is suggestive of the presence of a large-scale coherent structure in the flow field. The selected region of interest shown in (I-*b*), enclosed by a yellow square is the same as the region of interest chosen for the case of combustion noise. The large-scale structure is captured within the chosen region of interest. The flame contour from the Mie scattering images are shown in (II) along with the estimated values of D_0 and α_0. The acoustic pressure fluctuations corresponding to these Mie scattering images are marked in (III).

4.3. *Multifractal analysis of the flame during thermoacoustic instability*

We present the instantaneous Mie scattering images acquired during one cycle of thermoacoustic instability ($\phi = 0.6$) in figure 8(I). The corresponding flame contours in the region of interest are shown in figure 8(II). The spatial dynamics of the flame during the occurrence of thermoacoustic instability exhibits similar characteristics to that of the periodic epochs of intermittency. During this state, the unsteady heat release rate fluctuations associated with the large-scale coherent structures strongly interact with the acoustic field, which in turn, results in large amplitude periodic pressure oscillations (Poinsot *et al.* 1987; Ken, Trouve & Daily 1991; Hong *et al.* 2013). The formation of the large-scale coherent structure and the subsequent roll-up of the flame observed during one cycle of thermoacoustic instability can be observed in figure 8-I(*a–f*). The small-scale vortices present within the large-scale vortex cause the flame to be highly wrinkled and irregular. This presence of wrinkles of multiple length scales requires a broader range of scaling exponents to describe the flame dynamics.

Figure 9(*a*) depicts the temporal variation of D_0 during the occurrence of thermoacoustic instability. The maximum and minimum values of D_0 are 1.81 and 1.28, respectively, with a mean of 1.59. This suggests that the space-filling nature of the flame is restricted to certain instants of the periodic cycle where the values of D_0 are high. The maximum value of D_0 is higher than those observed during combustion noise and intermittency. The overall increase in the value of D_0 during the occurrence of thermoacoustic instability indicates that the flame occupies a larger area of the region of interest. This is due to the existence of large-scale roll up of the flame and the presence of small-scale wrinkles within the large-scale roll up (refer figure 8-II). In addition, we can also observe that the temporal modulation of D_0 is nearly periodic. This is due to the periodic emergence of the large-scale coherent structures, similar to the periodic epochs of intermittency.

The temporal variation of α_0 and the corresponding p' and $\dot{q}'$ are shown in figures 9(*b*) and 9(*c*), respectively. The value of α_0 oscillates around a mean value of 1.64. The maximum and minimum values of α_0 are 1.87 and 1.31, respectively. The range of D_0 and α_0 is larger compared to those during the occurrence of intermittency and combustion noise. The instances of the occurrence of lowest and highest value of α_0 correspond to the occurrence of lowest and highest values of D_0, respectively (also seen for combustion noise and intermittency). This indicates that α_0 is correlated to D_0. Both D_0 and α_0 reach their maximum values at the instant when the coherent structure reaches its maximum size, before impingement on the bluff-body.

We show the variation of multifractal spectrum for different instants of time during one acoustic cycle of thermoacoustic instability in figure 9(*d*) for the sequence of flames shown in figure 8(II). The mean value of the width of the multifractal spectrum is 0.35 during the occurrence of thermoacoustic instability, which is higher than the mean value of W (0.28) observed for the other dynamical states. Even though the multifractal spectrum is right-skewed for all flames, the skewness is less for flames corresponding to the curves (*b–d*). This reduction in the skewness of the right half of the spectrum for this set of flame contours suggests a lower irregularity at the smaller scales. Further, along with D_0 and α_0, the multifractal spectrum also oscillates periodically at the time scale at which coherent structures are formed in the flow field. This periodic oscillation of multifractal spectrum of the flame topology corresponds to the periodic oscillations in the heat release rate and the acoustic pressure fluctuations.

In our study, we compared the multifractal characteristics of flame contours obtained on a 2-D plane during different dynamical states. We showed that the multifractal

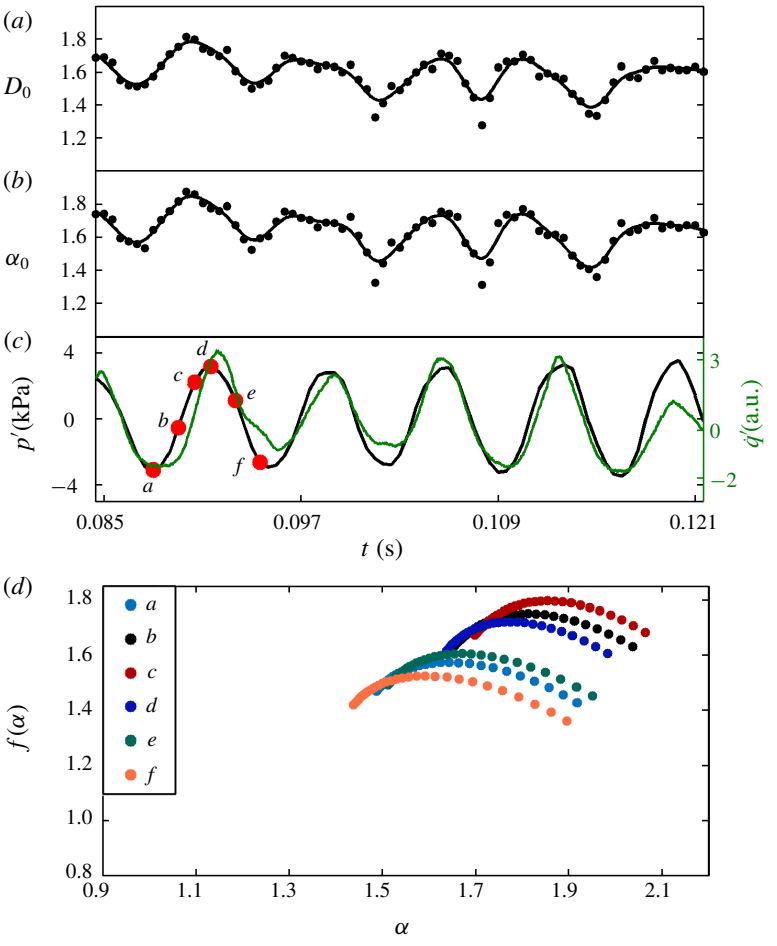

FIGURE 9. Time trace of D_0 (*a*), α_0 (*b*) and the corresponding p' (black line) with $\dot{q}'$ (green line) (*c*) during the occurrence of thermoacoustic instability is shown. Here, D_0 and α_0 oscillate periodically with the same time scale at which acoustic pressure oscillates. The maximum value of $\dot{q}'$ occurs after the breaking of a large-scale coherent structure into small-scale structures and the subsequent release of heat. The variation of the multifractal spectra at different instances during one acoustic cycle of thermoacoustic instability are shown in (*d*).

spectrum remains almost constant during the state of combustion noise. On the other hand, the multifractal spectrum oscillates periodically during the occurrence of thermoacoustic instability. From the analysis of 2-D images of the flame, we can make reasonable assumptions of the variation in the multifractal spectrum corresponding to the three-dimensional (3-D) flame. During the occurrence of combustion noise, we expect that small-scale structures exist throughout the 3-D flame. The value of D_0 for combustion noise would be lower than that obtained for thermoacoustic instability. We expect that the difference between the measures obtained for combustion noise and thermoacoustic instability would be larger when the 3-D flames are investigated. This is because the addition of the azimuthal direction would result in an additional scale for the state of thermoacoustic instability and increase D_0. On the other hand, α_0 would remain nearly the same for a 3-D flame as observed for a 2-D flame,

provided that the distribution of the small scale structures is invariant with respect to the azimuthal direction. Based on the points listed above, we hypothesize that the analysis of a 3-D flame would lead to similar conclusions while comparing the different dynamical states.

In a multifractal analysis, the singularity exponent α is described based on the distribution of a measure in the field. Thus, a change in the spatial distribution of measure would result in additional singularity exponents in the system. For instance, a non-axisymmetric flame would result in additional scales in the system and thereby change the distribution of the measure and affect the multifractal spectrum.

Though the scaling nature may differ for an axisymmetric and non-axisymmetric flame, the multifractal characteristics demonstrated by the flame during different dynamical states are preserved. This is owing to the fact that the thermoacoustic instability is characterized by the periodic emergence of large-scale coherent structures, which results in periodic oscillations of the multifractal spectrum. Similarly, highly unorganized small-scale structures govern the flame during the state of combustion noise and results in a non-varying multifractal spectrum.

It is important to highlight how the multifractal analysis of the flame can be applied to practical applications. Modelling the heat release rate of the turbulent thermoacoustic system with existing computational methodologies such as direct numerical simulation (known as DNS) and large eddy simulation (known as LES) is difficult as it involves expensive computation and validation of the models. Obtaining transfer functions (flame transfer function and flame describing function) to model the heat release rate response is quite expensive as it requires inputs from rigourous experiments. The observation of multifractality due to flame wrinkling during various regimes of combustor operation indicates that multiplicative processes associated with the turbulent reactive flow govern the heat release rate. The rules governing these multiplicative processes are inherently very simple (Meneveau & Sreenivasan 1987; Sreenivasan 1991). Thus, it may be instructive to model the heat release rate through these multiplicative processes. A first approach would be to develop a heat release rate model which depends on the capacity dimension (D_0) of the flame for premixed flamelets (Peters 2000). Doing so will implicitly introduce the effect of turbulence in the acoustic wave equation, typically solved in thermoacoustic instability, through the source term.

5. Conclusion

In a turbulent thermoacoustic system, Nair & Sujith (2014) showed a loss of multifractality due to the reduction of multiple temporal scales of pressure fluctuations to a few discrete temporal scales, when the thermoacoustic system transitions from combustion noise to thermoacoustic instability. Interestingly, our study reveals that in the spatial domain, multifractality is omnipresent as the dynamical state transitions from combustion noise to thermoacoustic instability via intermittency. The increase in the capacity dimension during the transition to thermoacoustic instability indicates an increase in the space-filling nature of the flame. The space-filling nature of the flame is periodic in time, which gives rise to periodic oscillations of the heat release rate during thermoacoustic instability. We suggest that it is this periodic space-filling nature of the flame, due to the flow-flame interaction, which results in the emergence of spatiotemporal order and coherence in the acoustic power production during thermoacoustic instability.

Further, at the onset of thermoacoustic instability, the periodic temporal evolution of large-scale coherent structures manifests as periodic oscillations of the multifractal

spectrum. During these periodic oscillations of the multifractal spectrum, we have seen that both D_0 and α_0 oscillate periodically with time. We observe that both D_0 and α_0 reach their maximum values at the instant when the coherent structure reaches its maximum size, before impingement on the bluff-body. Thus, the flame has the maximum surface area at this time. This maximum surface area is achieved due to the presence of several small-scale vortices within the large-scale coherent structure. George *et al.* (2018) suggested that the interaction of small-scale vortices to form a large-scale vortex, termed as collective interaction, results in the emergence of coherence in the acoustic power production at the onset of thermoacoustic instability. We are able to describe the increase in the wrinkling of the flame using fractal/multifractal measures, and relate it to the periodic heat release rate oscillations that happen in this complex turbulent flow field.

It is worth noting that through the use of multifractal formalism we can relate the loss of chaos and loss of multifractality in the time series of acoustic pressure with the increasingly complex spatial topology of the flame during the transition to thermoacoustic instability. As a final remark, developing a phenomenological model which relates the complex spatial flame topology to the complex dynamics of the acoustic pressure during the transition to thermoacoustic instability through a fractal or multifractal formalism would enable us to capture the fundamental processes involved in the problem.

Acknowledgements

The authors wish to thank Siemens Technology and Services Pvt. Ltd. for funding the project. We acknowledge Dr R. Richardson (Siemens Technology and Services Pvt. Ltd.) for his constant interaction with us from the commencement of the project. We would also like to thank Mr V. Hande and Dr R. S. Kaluri (Siemens Technology and Services Pvt. Ltd.) for their continuous support during the project. The authors wish to thank Mr S. Thilagaraj and Mr S. Anand (Indian Institute of Technology Madras) for their support in performing the experiments. We also thank our colleagues from the Indian Institute of Technology Madras, Mr K. Praveen, Ms V. Godavarthi, Ms P. Induja, Mr A. Roy and Mr A. J. Varghese for their critical comments and suggestions. N.B.G. acknowledges the support of the East Africa Peru India Climate Capacities (EPICC) project (18_11_149_Global_A_Risikovorhersage) funded by the Federal Ministry for the Environment, Nature Conservation and Nuclear Safety (BMU), and the funding from Deutscher Akademischer Austauschdienst (DAAD) for a research visit to IIT Madras in December 2018.

Declaration of interests

The authors report no conflict of interest.

Appendix A. Comparison of spatial length scales

In general, there are different spatial scales present in the turbulent reactive flow, ranging from the Kolmogorov's length scale η to the largest eddy scale referred to as the integral length scale l_0. The different spatial scales associated with flame roll-up observed across different dynamical states are small-scale flame roll-up ($\delta \sim 2$ mm), medium-scale roll-up ($M \sim 6$ mm) and large-scale roll-up ($L \sim 15$ mm) as described in § 4.

The flame roll-up contours are extracted from the 2-D Mie scattering images acquired using the digital camera with spatial resolution of 20 pixels mm^{-1} and thus 1 pixel corresponds to $l_c = 0.05$ mm. The extracted flame contours have a maximum thickness $l_t \approx 0.1$ mm. Noting that $\delta/l_t \approx 20$ and $\delta/l_c \approx 40$, the range of the extracted flame roll-ups are sufficiently resolved in our analysis.

The integral length scale l_0 is typically of the order of the characteristic length scale of the system, which is the step size of the combustor ($l_0 \approx l_s = 25$ mm). Assuming Kolmogorov's hypothesis of local isotropy holds, η is related to l_0 as

$$\eta \sim l_0 \times Re^{-3/4}. \tag{A 1}$$

For the reported range of Reynolds number, $Re = 1.88 \times 10^4$ to 3.15×10^4, and $l_0 \approx 25$ mm, the Kolmogorov length scale is in the range $\eta \sim 0.01 - 0.016$ mm. By comparing the small-scale flame roll-up ($\delta \sim 2$ mm) with Kolmogorov's length scale $\eta \sim 0.01$ mm and large-scale flame roll-up ($L \sim 15$ mm) with integral length scale l_0, we obtain $\eta/\delta \sim 200$ and $L/l_0 \sim 3/5$. Thus, by substituting η and l_0 in terms of δ and L, respectively, equation (A 1) is modified as

$$\frac{L}{\delta} \sim \frac{3}{1000} Re^{-3/4}. \tag{A 2}$$

The above expression gives an empirical relation between the largest and smallest scales associated with flame roll-ups observed during different states of combustor operation.

Appendix B. Edge detection technique to detect the flame contour from the Mie scattering images

Proper identification of the flame contour is necessary for the multifractal analysis (Shepherd, Cheng & Talbot 1992; Foroutan-pour, Dutilleul & Smith 1999). The acquired Mie scattering images of the flame are converted into binary images to obtain the flame contour. The raw Mie scattering images are converted into binary images through the following steps.

(i) Background correction is performed to reduce background noise and high reflection caused by the laser.

(ii) The greyscale images are initially binarized using Otsu's thresholding method with suitable threshold to give a preliminary flame boundary (Ostu 1979).

(iii) This flame boundary is then smoothed (Shepherd *et al.* 1992; Foroutan-pour *et al.* 1999). Image smoothing is achieved by using a dilation function on the binary image with an appropriate threshold (Gonzalez, Woods & Eddins 2004). The dilation function operates on the binary image to enlarge the area of the flame boundary. Subsequently, this step reduces the area represented by the non-boundary regions close to the flame boundary.

(iv) The dilated image is then skeletonized to get a uniformly thin flame boundary whose width occupies only one pixel (Lam, Lee & Suen 1992).

(v) Smaller and isolated circular objects could also be detected along with the flame as a result of the previous steps. These isolated circular objects are then removed by providing a threshold based on the area.

During the occurrence of thermoacoustic instability, multiple small-scale spatial structures exist within the large-scale spatial structures. To capture the boundary of all these spatial structures, the dilation threshold (step (iii)) is applied locally based on the pixel intensities.

Appendix C. Evaluation of singularity exponent (α) and the multifractal spectrum ($f(\alpha)$)

Before examining the procedure for the evaluation of the singularity spectrum, let us examine the concept of a measure. A measure (μ) can be thought of as a function which takes in a set as the input variable and maps it to a non-negative real number. This is denoted mathematically as $\mu : S \rightarrow [0, \infty)$ where S is the set. One can think of the Lebesgue measure to understand this concept better. Given a set, the Lebesgue measure is defined as the volume of this set. One is free to define the measure for a set, provided it satisfies the following conditions.

(i) Non-negativity: measure has to be a non-negative real number, i.e., $\mu(T) \geqslant 0 \, \forall \, T \in S$.

(ii) Countable additivity: the measure of a countable union of disjoint sets is the sum of the measure of each set, i.e., $\mu(\bigcup_{i=1}^{n} T_i) = \sum_{i=1}^{n} \mu(T_i)$.

In practice, the spatial field G (which is the flame contour in our study) is considered as a set on which the measure μ is defined by satisfying the above conditions. In our analysis, μ is selected as the normalized probability mass distribution of the non-zero pixel intensity in the flame contours (Giri *et al.* 2014). After detection of the flame contour, we calculate the probability distribution P of the number of pixels intensities M present in each box of size ε that is needed to cover the flame contour,

$$P_i(\varepsilon) = \frac{M_i(\varepsilon)}{\sum_{i=1}^{N(\varepsilon)} M_i(\varepsilon)}. \tag{C 1}$$

Here, $N(\varepsilon)$ is the total number of boxes of size ε that contain the pixels. The measure μ is given as

$$\mu_i(q, \varepsilon) = \frac{P_i(\varepsilon)^q}{\sum_{i=1}^{N(\varepsilon)} P_i(\varepsilon)^q}, \tag{C 2}$$

where q is the order of moment of the measure. According to Chhabra & Jensen (1989), the singularity exponent α and the multifractal spectrum $f(\alpha)$ are calculated as

$$\alpha(q) = \lim_{\varepsilon \to 0} \frac{\sum_{i=1}^{N(\varepsilon)} \mu_i(q, \varepsilon) \ln P_i(\varepsilon)}{\ln \varepsilon}, \tag{C 3}$$

$$f(\alpha) = \lim_{\varepsilon \to 0} \frac{\sum_{i=1}^{N(\varepsilon)} \mu_i(q, \varepsilon) \ln \mu_i(q, \varepsilon)}{\ln \varepsilon}. \tag{C 4}$$

For each value of q, we plot $\sum \mu_i(q, \varepsilon) \ln P_i(\varepsilon)$ versus $\ln \varepsilon$ and $\sum \mu_i(q, \varepsilon) \ln \mu_i(q, \varepsilon)$ versus $\ln \varepsilon$. The slopes of the linear fit for these two plots provide the values of α and $f(\alpha)$, respectively. The best linear fit is achieved for a specific range of q (Puthenveettil, Ananthakrishna & Arakeri 2005). We apply the above-mentioned algorithm to the image of a flame shown in figure 10(*a*).

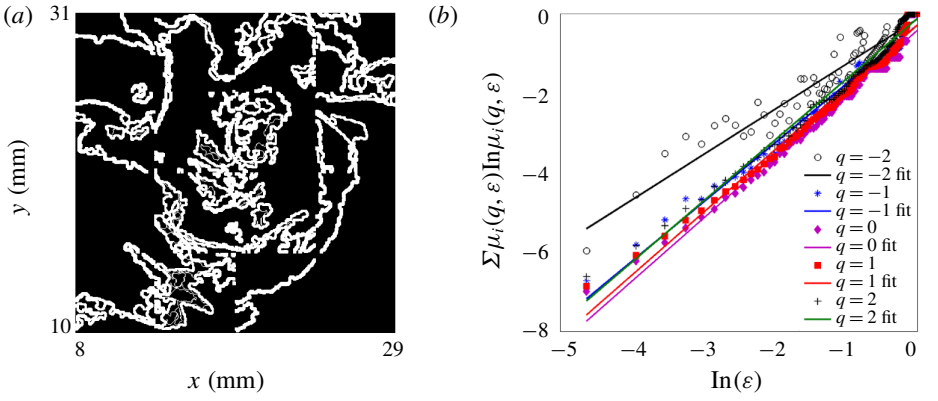

FIGURE 10. The detected flame contour from the Mie scattering image of the flame is shown in (*a*). The range of $f(\alpha)$ calculated for different q values from -2 to 2 are shown in (*b*). The different lines represent the linear fits for different values of q.

Figure 10(*b*) depicts the logarithmic variation of measure μ with box size ε used to estimate $f(\alpha)$ for the flame shown in figure 10(*a*). In figure 10(*b*), we observe that there is a deviation in the linear fitted curve plotted for $q < -1$. Similarly a deviation is also observed for q greater than 2 (not shown here). In our work, the range of q values is restricted to $-1 \leqslant q \leqslant 2$ in order to have a reasonable range of scaling regime.

In the above described box-counting method, we did not use the Legendre transformation to estimate $f(\alpha)$ and α. Other methods such as the wavelet transform method use the Legendre transformation to calculate $f(\alpha)$ and α. The multifractal spectrum calculated using Legendre transformation involves a higher uncertainty for the negative q values (Chhabra & Jensen 1989; Veneziano, Moglen & Bras 1995). Avoiding the usage of the Legendre transformation of $\tau(q)$ increases the accuracy of the multifractal spectrum calculated from the box-counting method used here. In our study, the dynamics of the flame front is suitably represented in a binary form. The box-counting method estimates the multifractal spectrum in a more accurate manner for binarized signals with less computational time (Lopes & Betrouni 2009). Thus, the box-counting method is adopted in our current analysis.

Normant & Tricot (1991) reported that the box-counting technique is valid only for statistically self-similar signals. However, it has been shown that natural objects exhibit statistical self-similarity only for a finite range of scales $[\varepsilon_{min}\ \varepsilon_{max}]$ considered in the box-counting method (Beauvais & Montgomery 1997). By considering a finite range of scales for which statistical self-similarity is preserved, the dynamics due to other scales would be lost (Beauvais & Montgomery 1997; Tanner, Perfect & Kelley 2006). By considering all scales, the natural objects demonstrate that the space-filling nature is preserved even in the absence of statistical self-similarity (Beauvais & Montgomery 1997). In our study, we have a range of scales associated with the size of flame roll-up as discussed in § 4. We need to take into account the entire range of scales because of their physical relevance in relation to the size of the vortices. By considering the entire range of scales in the box-counting analysis, the flame is not statistically self-similar. However, the flame exhibits the space-filling nature when all scales are taken into account. This space-filling nature supports the occurrence of an

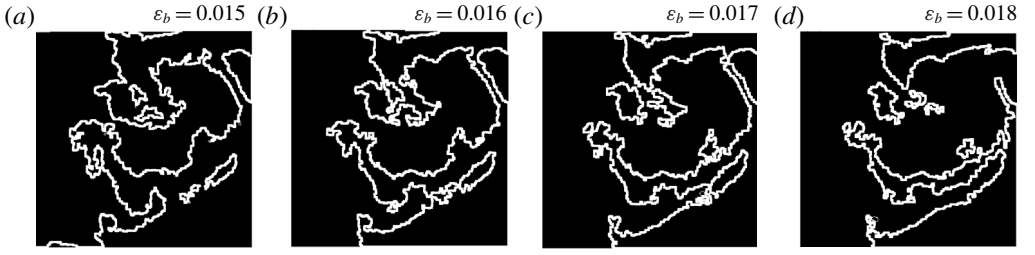

FIGURE 11. The extracted flame contours for different thresholds (*a*) $\varepsilon_b = 0.015$, (*b*) $\varepsilon_b = 0.016$, (*c*) $\varepsilon_b = 0.017$ and (*d*) $\varepsilon_b = 0.018$ are shown here. The flame contours extracted are almost the same for all ε_b values.

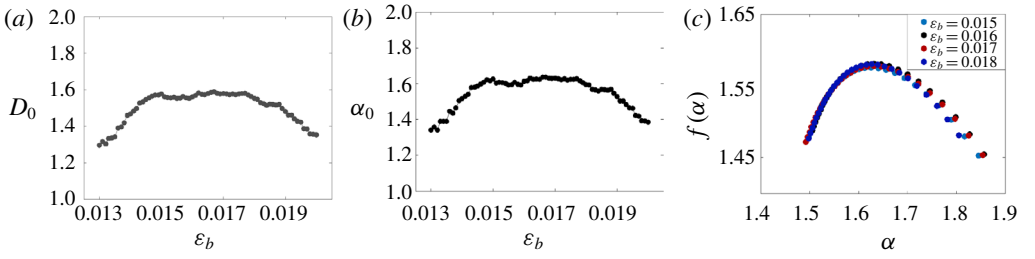

FIGURE 12. The variation of the capacity dimension D_0 (*a*), the most dominant singularity exponent α_0 (*b*) and the multifractal spectrum (*c*) for different binarization thresholds are shown. The multifractal parameters show almost the same value in the range of ε_b between 0.015 and 0.018.

intense field of heat release rate during the presence of large-scale coherent structure. Thus, we continue to use the box-counting method considering all the flow scales for the estimation of fractal dimension.

Appendix D. Uncertainties in the multifractal spectrum

Though the box-counting method has advantages in the estimation of the multifractal spectrum for the binary images, there are uncertainties which arise due to the improper selection of thresholds during the image-processing (Shepherd *et al.* 1992; Foroutan-pour *et al.* 1999) and also due to the use of linear curve fit to calculate the slope (Górski *et al.* 2012). At first, we examine uncertainties associated with the usage of different thresholds in the extraction of the flame contours. There are uncertainties associated with the usage of different thresholds in the extraction of the flame contours. We binarize the Mie scattering image using Otsu's thresholding method (Ostu 1979) using an optimal binarization threshold. In order to find the optimal threshold, we vary the binarization threshold ε_b from 0.01 to 0.02. The extracted flame contours for four different thresholds, $\varepsilon_b = 0.015$, $\varepsilon_b = 0.016$, $\varepsilon_b = 0.017$ and $\varepsilon_b = 0.018$ are shown in figure 11(*a–d*), respectively. From figure 11(*a–d*), we can observe that the extracted contours are nearly the same for these ε_b values.

The multifractal parameters namely D_0, α_0 and the multifractal spectrum corresponding to different threshold values of ε_b are shown in figure 12(*a–c*). From

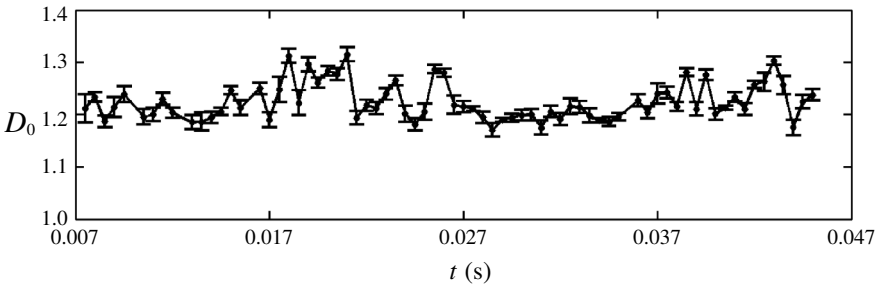

FIGURE 13. Time trace of D_0 along with error bars during the occurrence of combustion noise.

figure 12(*a–c*), we can observe that D_0, α_0 and the multifractal spectrum are almost constant for the range of ε_b from 0.015 to 0.018. Thus, we use ε_b of 0.0165 for the extraction of flame contours throughout the multifractal analysis for the state of intermittency. The same procedure is followed for the analysis of flame images captured during the state of combustion noise and thermoacoustic instability.

The optimal threshold for the dilation function is determined in the same manner as that for obtaining the optimal threshold for Otsu's binarization scheme. We find the values of the threshold for which multifractal characteristics remain constant, and then chose the appropriate threshold value.

The uncertainty in the estimation of $f(\alpha)$ and α due to the use of linear curve fit to calculate the slope is explained as follows. The linear curve fitting algorithm optimizes the constants of a fitting equation by minimizing the sum of the squares of deviations of the actual (data) values from the values predicted by the equation. The uncertainty is calculated from the difference between the actual data and the fitted data by using the following equation (Coleman & Steele 2018):

$$S_e = \sqrt[2]{\frac{\sum_{i=1}^{N(\varepsilon)} y^2 - b_p \sum_{i=1}^{N(\varepsilon)} y - b_m \sum_{i=1}^{N(\varepsilon)} xy}{N(\varepsilon) - 2}}. \tag{D 1}$$

Here, y is $\log(\mu)$ and x is $\log(\varepsilon)$. The intercept and the slope of the fitted line are given by b_p and b_m, respectively.

To find the goodness of the fitted values, we find their confidence interval. The confidence interval for b_m is given as

$$b_m \pm t_c \frac{S_e}{\sqrt[2]{\sum_{i=1}^{N(\varepsilon)} x^2 - N(\varepsilon)\bar{x}^2}}, \tag{D 2}$$

where t_c is the set of values which depend upon on the percentage of the confidence interval for which we calculate the goodness of the fitted values.

By considering a 90 % confidence interval, we calculate the uncertainty in the estimation of D_0 during the occurrence of combustion noise as shown in figure 13. The same procedure is followed to calculate the uncertainty for all multifractal

Dynamical states	D_0	α_0
Combustion noise	± 0.024	± 0.027
Aperiodic epochs of intermittency	± 0.04	± 0.038
Periodic epochs of intermittency	± 0.068	± 0.049
Thermoacoustic instability	± 0.067	± 0.083

TABLE 1. Uncertainties in the calculation of parameters of the multifractal spectrum for different dynamical states.

parameters used in our study and is tabulated in table 1. Low values of uncertainty are obtained for D_0 and α_0.

REFERENCES

AREF, H. 1983 Integrable, chaotic, and turbulent vortex motion in two-dimensional flows. *Annu. Rev. Fluid Mech.* **15** (1), 345–389.

BALL, P. 1999 *The Self-Made Tapestry: Pattern Formation in Nature*. Oxford University Press.

BEAUVAIS, A. A. & MONTGOMERY, D. R. 1997 Are channel networks statistically self-similar? *Geology* **25** (12), 1063–1066.

BENZI, R., CILIBERTO, S., TRIPICCIONE, R., BAUDET, C., MASSAIOLI, F. & SUCCI, S. 1993 Extended self-similarity in turbulent flows. *Phys. Rev.* E **48**, R29–R32.

CAMAZINE, S., DENEUBOURG, J. L., FRANKS, N. R., SNEYD, J., BONABEAU, E. & THERAULA, G. 2003 *Self-Organization in Biological Systems*. Princeton University Press.

CANDEL, S. M. 1992 Combustion instabilities coupled by pressure waves and their active control. In *Symposium (International) on Combustion*, vol. 24, pp. 1277–1296. Elsevier.

CHENG, Q. 2014 Generalized binomial multiplicative cascade processes and asymmetrical multifractal distributions. *Nonlinear Process. Geophys.* **21** (2), 477–487.

CHHABRA, A. & JENSEN, R. V. 1989 Direct determination of the $f(\alpha)$ singularity spectrum. *Phys. Rev. Lett.* **62**, 1327–1330.

CIOTTI, L., BUDRONI, M. A., MASIA, M., MARCHETTINI, N. & RUSTICI, M. 2011 Competition between transport phenomena in a reaction–diffusion–convection system. *Chem. Phys. Lett.* **512** (4-6), 290–296.

COLEMAN, H. W. & STEELE, W. G. 2018 *Experimentation, Validation, and Uncertainty Analysis for Engineers*. Wiley.

CROSS, M. C. & HOHENBERG, P. C. 1993 Pattern formation outside of equilibrium. *Rev. Mod. Phys.* **65**, 851–1112.

DAUPHINÉ, A. 2013 *From the Fractal Dimension to Multifractal Spectrums*, chap. 3, pp. 39–57. Wiley Online Library.

DAVIDSON, P. 2015 *Turbulence: An Introduction for Scientists and Engineers*. Oxford University Press.

ENGELKING, R. 1978 *Dimension Theory*. North-Holland.

FOROUTAN-POUR, K., DUTILLEUL, P. & SMITH, D. L. 1999 Advances in the implementation of the box-counting method of fractal dimension estimation. *Appl. Maths Comput.* **105** (2–3), 195–210.

FRISCH, U. & KOLMOGOROV, A. N. 1995 *Turbulence: The Legacy of A. N. Kolmogorov*. Cambridge University Press.

FUNG, Y. C. 1955 *An Introduction to the Theory of Aeroelasticity*. Wiley.

GEORGE, N. B., UNNI, V. R., RAGHUNATHAN, M. & SUJITH, R. I. 2018 Pattern formation during transition from combustion noise to thermoacoustic instability via intermittency. *J. Fluid Mech.* **849**, 615–644.

GIRI, A., TARAFDAR, S., GOUZE, P. & DUTTA, T. 2014 Multifractal analysis of the pore space of real and simulated sedimentary rocks. *Geophys. J. Intl* **200** (2), 1108–1117.

GOLTZ, C. 1996 Multifractal and entropic properties of landslides in Japan. *Geol. Rundsch.* **85** (1), 71–84.

GONZALEZ, R. C., WOODS, R. E. & EDDINS, S. L. 2004 *Digital Image Processing Using MATLAB*. pp. 349–438. Pearson.

GÓRSKI, A. Z., DROZDZ, S., MOKRZYCKA, A. & PAWLIK, J. 2012 Accuracy analysis of the box-counting algorithm. In *Proceedings of the 5th Symposium on Physics in Economics and Social Sciences, Warszawa, Poland, November 25–27, 2010*. APP.

GOTODA, H., AMANO, M., MIYANO, T., IKAWA, T., MAKI, K. & TACHIBANA, S. 2012 Characterization of complexities in combustion instability in a lean premixed gas-turbine model combustor. *Chaos* **22** (4), 043128.

GOTODA, H., NIKIMOTO, H., MIYANO, T. & TACHIBANA, S. 2011 Dynamic properties of combustion instability in a lean premixed gas-turbine combustor. *Chaos* **21** (1), 013124.

GOTODA, H., OKUNO, Y., HAYASHI, K. & TACHIBANA, S. 2015 Characterization of degeneration process in combustion instability based on dynamical systems theory. *Phys. Rev.* E **92**, 052906.

GÜLDER, Ö. L., SMALLWOOD, G. J., WONG, R., SNELLING, D. R., SMITH, R., DESCHAMPS, B. M. & SAUTET, J. C. 2000 Flame front surface characteristics in turbulent premixed propane/air combustion. *Combust. Flame* **120** (4), 407–416.

HARDALUPAS, Y. & ORAIN, M. 2004 Local measurements of the time-dependent heat release rate and equivalence ratio using chemiluminescent emission from a flame. *Combust. Flame* **139** (3), 188–207.

HO, C. M. & NOSSEIR, N. S. 1981 Dynamics of an impinging jet. Part 1. The feedback phenomenon. *J. Fluid Mech.* **105**, 119–142.

HOLMAN, J. P. 1989 *Heat Transfer*. McGraw-Hill.

HONG, S., SPETH, R. L., SHANBHOGUE, S. J. & GHONIEM, A. F. 2013 Examining flow-flame interaction and the characteristic stretch rate in vortex-driven combustion dynamics using PIV and numerical simulation. *Combust. Flame* **160** (8), 1381–1397.

IHLEN, E. A. & VEREIJKEN, B. 2013 Multifractal formalisms of human behavior. *Human Movement Sci.* **32** (4), 633–651.

IVANOV, P. CH., AMARAL, L. A. N., GOLDBERGER, A. L., HAVLIN, S., ROSENBLUM, M. G., STRUZIK, Z. R. & STANLEY, H. E. 1999 Multifractality in human heartbeat dynamics. *Sensors Actuators* A **399**, 461.

JUNIPER, M. P. & SUJITH, R. I. 2018 Sensitivity and nonlinearity of thermoacoustic oscillations. *Annu. Rev. Fluid Mech.* **50** (1), 661–689.

KELLER, J. O., VANEVELD, L., KORSCHELT, D., HUBBARD, G. L., GHONIEM, A. F., DAILY, J. W. & OPPENHEIM, A. K. 1982 Mechanism of instabilities in turbulent combustion leading to flashback. *AIAA J.* **20** (2), 254–262.

KEN, H. Y., TROUVE, A. & DAILY, J. W. 1991 Low-frequency pressure oscillations in a model ramjet combustor. *J. Fluid Mech.* **232**, 47–72.

KIM, M., CHOI, Y., OH, J. & YOON, Y. 2009 Flame–vortex interaction and mixing behaviors of turbulent non-premixed jet flames under acoustic forcing. *Combust. Flame* **156** (12), 2252–2263.

LAM, L., LEE, S.-W. & SUEN, C. Y. 1992 Thinning methodologies – a comprehensive survey. *IEEE Trans. Pattern Anal. Mach. Intell.* **14** (9), 869–885.

LIEUWEN, T. C. 2012 *Unsteady Combustor Physics*. Cambridge University Press.

LOPES, R. & BETROUNI, N. 2009 Fractal and multifractal analysis: a review. *Med. Image Anal.* **13** (4), 634–649.

LOVEJOY, S. & SCHERTZER, D. 1991 *Multifractal Analysis Techniques and the Rain and Cloud Fields*, pp. 111–144. Springer.

MANDELBROT, B. B. 1974 Intermittent turbulence in self-similar cascades: divergence of high moments and dimension of the carrier. *J. Fluid Mech.* **62** (2), 331–358.

MANDELBROT, B. B. 1983 *The Fractal Geometry of Nature*. W. H. Freeman.

MANDELBROT, B. B. 1989 Multifractal measures, especially for the geophysicist. *Pure Appl. Geophys.* **131**, 5–42.

MARTÍNEZ, V. J., JONES, B. J., DOMÍNGUEZ-TENREIRO, R. & WEYGAERT, R. 1990 Clustering paradigms and multifractal measures. *Astrophys. J.* **357**, 50.

MCWILLIAMS, J. C. 1984 The emergence of isolated coherent vortices in turbulent flow. *J. Fluid Mech.* **146**, 21–43.

MENEVEAU, C. & SREENIVASAN, K. R. 1986 The fractal facets of turbulence. *J. Fluid Mech.* **173**, 357–386.

MENEVEAU, C. & SREENIVASAN, K. R. 1987 Simple multifractal cascade model for fully developed turbulence. *Phys. Rev. Lett.* **59** (13), 1424.

MENEVEAU, C. & SREENIVASAN, K. R. 1991 The multifractal nature of turbulent energy dissipation. *J. Fluid Mech.* **224**, 429–484.

MONDAL, S., UNNI, V. R. & SUJITH, R. I. 2017 Onset of thermoacoustic instability in turbulent combustors: an emergence of synchronized periodicity through formation of chimera-like states. *J. Fluid Mech.* **811**, 659–681.

MURCIO, R., MASUCCI, A. P., ARCAUTE, E. & BATTY, M. 2015 Multifractal to monofractal evolution of the London street network. *Phys. Rev.* E **92**, 062130.

NAIR, S. & LIEUWEN, T. C. 2007 Near-blowoff dynamics of a bluff-body stabilized flame. *J. Propul. Power* **23** (2), 421–427.

NAIR, V. & SUJITH, R. I. 2014 Multifractality in combustion noise: predicting an impending combustion instability. *J. Fluid Mech.* **747**, 635–655.

NAIR, V., THAMPI, G. & SUJITH, R. I. 2014 Intermittency route to thermoacoustic instability in turbulent combustors. *J. Fluid Mech.* **756**, 470–487.

NORMANT, F. & TRICOT, C. 1991 Method for evaluating the fractal dimension of curves using convex hulls. *Phys. Rev.* A **43** (12), 6518.

NORTH, G. L. & SANTAVICCA, D. A. 1990 The fractal nature of premixed turbulent flames. *Combust. Sci. Technol.* **72** (4-6), 215–232.

OSTU, N. 1979 A threshold selection method from gray-level histograms. *IEEE Trans. Syst. Man Cybern.* **9** (1), 62–66.

PAWAR, S. A., SESHADRI, A., UNNI, V. R. & SUJITH, R. I. 2017 Thermoacoustic instability as mutual synchronization between the acoustic field of the confinement and turbulent reactive flow. *J. Fluid Mech.* **827**, 664–693.

PESIN, Y. B. 2008 *Dimension Theory in Dynamical Systems: Contemporary Views and Applications*. University of Chicago Press.

PETERS, N. 2000 *Turbulent Combustion*. Cambridge University Press.

POINSOT, T. J., TROUVE, A. C., VEYNANTE, D. P., CANDEL, S. M. & ESPOSITO, E. J. 1987 Vortex-driven acoustically coupled combustion instabilities. *J. Fluid Mech.* **177**, 265–292.

POPE, S. B. 2000 *Turbulent Flows*. Cambridge University Press.

PREMCHAND, C. P., GEORGE, N. B., RAGHUNATHAN, M., UNNI, V. R., SUJITH, R. I. & NAIR, V. 2019 Lagrangian analysis of intermittent sound sources in the flow-field of a bluff-body stabilized combustor. *Phys. Fluids* **31** (2), 025115.

PUTHENVEETTIL, B. A., ANANTHAKRISHNA, G. & ARAKERI, J. H. 2005 The multifractal nature of plume structure in high-Rayleigh-number convection. *J. Fluid Mech.* **526**, 245–256.

RENARD, P. H., ROLON, J. C., THÉVENIN, D. & CANDEL, S. 1999 Investigations of heat release, extinction, and time evolution of the flame surface, for a nonpremixed flame interacting with a vortex. *Combust. Flame* **117** (1–2), 189–205.

RICHARDSON, L. F. 1922 *Weather Prediction by Numerical Process*. Cambridge University Press.

ROCKWELL, D. 1983 Oscillations of impinging shear layers. *AIAA J.* **21** (5), 645–664.

ROCKWELL, D. & NAUDASCHER, E. 1979 Self-sustained oscillations of impinging free shear layers. *Annu. Rev. Fluid Mech.* **11** (1), 67–94.

SALAT, H., MURCIO, R. & ARCAUTE, E. 2017 Multifractal methodology. *Physica* A **473**, 467–487.

SCHERTZER, D., LOVEJOY, S., SCHMITT, F., CHIGIRINSKAYA, Y. & MARSAN, D. 1997 Multifractal cascade dynamics and turbulent intermittency. *Sensors Actuators* A **5** (03), 427–471.

SHANBHOGUE, S., SHIN, D. H., HEMCHANDRA, S., PLAKS, D. & LIEUWEN, T. C. 2009 Flame-sheet dynamics of bluff-body stabilized flames during longitudinal acoustic forcing. *Proc. Combust. Inst.* **32** (2), 1787–1794.

SHEPHERD, I. G., CHENG, R. K. & TALBOT, L. 1992 Experimental criteria for the determination of fractal parameters of premixed turbulent flames. *Exp. Fluids* **13** (6), 386–392.

SREENIVASAN, K. R. 1991 Fractals and multifractals in fluid turbulence. *Annu. Rev. Fluid Mech.* **23** (1), 539–604.

STELLA, A., GUJ, G., KOMPENHANS, J., RICHARD, H. & RAFFEL, M. 2001 Three-components particle image velocimetry measurements in premixed flames. *Aerosp. Sci. Technol.* **5** (5), 357–364.

STRAHLE, W. C. 1978 Combustion noise. *Prog. Energy Combust. Sci.* **4** (3), 157–176.

TANNER, B. R., PERFECT, E. & KELLEY, J. T. 2006 Fractal analysis of Maine's glaciated shoreline tests established coastal classification scheme. *J. Coast. Res.* 1300–1304.

TELESCA, L., COLANGELO, G., LAPENNA, V. & MACCHIATO, M. 2003 Monofractal and multifractal characterization of geoelectrical signals measured in southern Italy. *Chaos Solitons Fractals* **18** (2), 385–399.

TELESCA, L., LOVALLO, M., MOLIST, J. M., MORENO, C. L. & MELÉNDEZ, R. A. 2015 Multifractal investigation of continuous seismic signal recorded at El Hierro volcano (Canary Islands) during the 2011–2012 pre- and eruptive phases. *Tectonophysics* **642**, 71–77.

TENNEKES, H. & LUMLEY, J. L. 1972 *A First Course in Turbulence*. MIT Press.

TIEZZI, E. B. P., PULSELLI, R. M., MARCHETTINI, N. & TIEZZI, E. 2008 Dissipative structures in nature and human systems. In *Design and Nature IV*, p. 293. WIT Press.

UNNI, V. R., KRISHNAN, A., MANIKANDAN, R., GEORGE, N. B., SUJITH, R. I., MARWAN, N. & KURTHS, J. 2018 On the emergence of critical regions at the onset of thermoacoustic instability in a turbulent combustor. *Chaos* **28** (6), 063125.

UNNI, V. R. & SUJITH, R. I. 2015 Multifractal characteristics of combustor dynamics close to lean blowout. *J. Fluid Mech.* **784**, 30–50.

UNNI, V. R. & SUJITH, R. I. 2017 Flame dynamics during intermittency in a turbulent combustor. *Proc. Combust. Inst.* **36** (3), 3791–3798.

VENEZIANO, D., MOGLEN, G. E. & BRAS, R. L. 1995 Multifractal analysis: pitfalls of standard procedures and alternatives. *Phys. Rev.* E **52** (2), 1387.

WAGON, S. 2010 *Mathematica® in Action: Problem Solving Through Visualization and Computation*. Springer.

WILKE, C. R. 1950 A viscosity equation for gas mixtures. *J. Chem. Phys.* **18** (4), 517–519.

ZUKOSKI, E. 1985 Combustion instability sustained by unsteady vortex combustion. In *21st Joint Propulsion Conference*, p. 1248. AIAA.